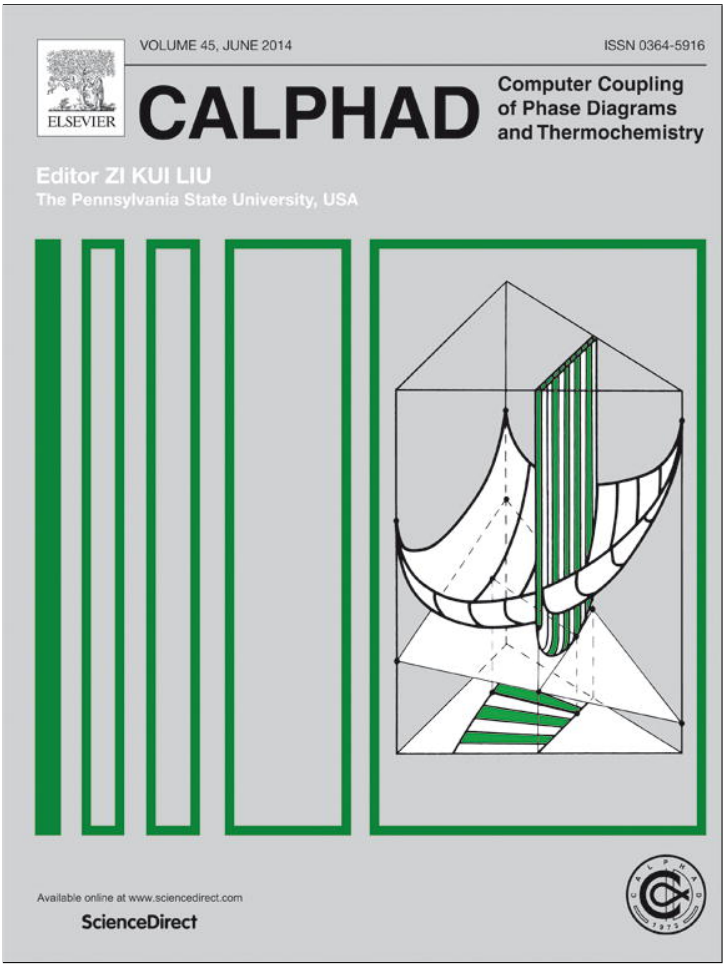

CALPHAD: Computer Coupling of Phase Diagrams and Thermochemistry 45 (2014) 33–39

Contents lists available at ScienceDirect

CALPHAD: Computer Coupling of Phase Diagrams and Thermochemistry

journal homepage: www.elsevier.com/locate/calphad

Cu–Ni nanoalloy phase diagram – Prediction and experiment

Jiri Sopousek [a,b,*], Jan Vrestal [a], Jiri Pinkas [a,b], Pavel Broz [a,b], Jiri Bursik [c], Ales Styskalik [a,b], David Skoda [a,b], Ondrej Zobac [a], Joonho Lee [d]

[a] Masaryk University, CEITEC MU, Brno, Czech Republic
[b] Masaryk University, Faculty of Sciences, Department of Chemistry, Brno, Czech Republic
[c] Institute of Physics of Materials ASCR Brno, Czech Republic
[d] Department of Materials Sciences and Engineering, Korea University, Seoul, Republic of Korea

ARTICLE INFO

Article history:
Received 16 April 2013
Received in revised form
6 November 2013
Accepted 8 November 2013
Available online 21 November 2013

Keywords:
Nanoalloy
Phase diagram
Thermodynamic modeling
Characterization
Surface energy

ABSTRACT

The Cu–Ni nanoalloy phase diagram respecting the nanoparticle size as an extra variable was calculated by the CALPHAD method. The samples of the Cu–Ni nanoalloys were prepared by the solvothermal synthesis from metal precursors. The samples were characterized by means of dynamic light scattering (DLS), infrared spectroscopy (IR), inductively coupled plasma optical emission spectroscopy (ICP/OES), transmission electron microscopy (TEM, HRTEM), and differential scanning calorimetry (DSC). The nanoparticle size, chemical composition, and Cu–Ni nanoparticles melting temperature depression were obtained. The experimental temperatures of melting of nanoparticles were in good agreement with the theoretical CALPHAD predictions considering surface energy.

1. Introduction

Nanoalloy phase diagrams differ substantially from the phase diagrams of bulk systems when the particle size (number of atoms) is included as an additional variable.

For the characterization of thermal stability, nanoalloy phase diagrams provide valuable information. The phase diagrams of nanoalloys, contrary to the ones of bulk, bring irreversible information because the equilibrium is attained during heating only. Reversibility is valid only for encapsulated nanoparticles (NPs). Melting behavior of the small Cu–Ni particles was modeled with thermodynamic approach (diameter over 60 nm) by Shirinyan et al. [1] and with molecular dynamic (size below 4 nm) by Huang and Balbuena [2]. Both models predict a depression of the solidus temperature, which is reported as size dependent. Nevertheless, the thermodynamic description of the larger systems (approx. >5 nm in radius in general) [3,4] respects general rules of thermodynamics and the phase diagrams can be calculated by the standard routes using surface energy contribution to the Gibbs energy of phases in the standard CALPHAD approach [5]. CALPHAD type calculations of phase diagrams are effective and useful tool for practical applications in the area of nanoalloys because thermodynamic data for various multi-component systems are available. First-principles approach is restricted to several hundred atoms and molecular dynamic simulations have their limitations when applied to multi-component systems. The CALPHAD type calculations make it possible to take the surface energy of nanoparticles into account and to calculate phase stability in this situation.

Park and Lee [6] have published a method to draw a nanophase diagram for public users who are familiar with user-friendly commercial software such as PANDAT [7], FactSage [8], MTDATA [9], Thermo-Calc [10], etc. This is made possible by describing the chemical potential of pure substances and the excess free energy as a function of temperature, composition and particle size. The method by Park and Lee [6] will be used in the present article for thermodynamic assessment of Cu–Ni system including the size effect. Certainly, a calculated phase diagram should denote the temperatures, for given composition, where melting of nanoparticles starts and ends during heating. Approximations used here are the same as in [1,6]: particles with diameter >10 nm, Cu and Ni are assumed to be perfectly mixed, T (temperature) is an appropriate parameter, no nucleation state is assumed.

Verification of calculations by the synthesis of Cu–Ni nanoparticles in water-in-oil microemulsion [11] and characterization of products by DLS, ICP/OES, TEM, HRTEM, IR and DSC contribute to the description of thermal stability of nanoalloys of Cu–Ni system.

2. Thermodynamic calculation of the Cu–Ni nanoalloy phase diagram

Nanoparticles have an increasing surface to volume ratio with decreasing particle size and bring therefore a substantial contribution

* Corresponding author at: Masaryk University, Faculty of Sciences, Department of Chemistry, Brno, Czech Republic. Tel.: +420 549497138.
E-mail address: sopousek@mail.muni.cz (J. Sopousek).

0364-5916/$ - see front matter © 2013 Elsevier Ltd. All rights reserved.
http://dx.doi.org/10.1016/j.calphad.2013.11.004

of the surface energy to the Gibbs energy in thermodynamic considerations. The surface contribution of the particles with diameters 5–100 nm can be estimated by thermodynamics coupled with surface contribution and the CALPHAD approach.

The chemical potential of pure substances and the excess Gibbs energy need to be described as a function of temperature, composition and particle size. The method, presented by Park and Lee [6] will be used in this work for calculation of the phase diagram of the Cu–Ni system.

The CALPHAD method used in [6] is based on the minimization of the molar Gibbs energy of the entire system, which is a sum of the molar Gibbs energy of the phases present in the system. The phase Gibbs energy is given by

$$G = G^{Bulk} + G^{S} \tag{1}$$

where G^{Bulk} is the Gibbs energies of the bulk binary alloy and G^{S} means the surface excess Gibbs energy contribution.

The Gibbs energy of the bulk G^{Bulk} is expressed by the standard CALPHAD way

$$G^{Bulk} = x_A {}^0G_A + x_B {}^0G_B + RT(x_A \ln x_A + x_B \ln x_B) + G^{E,Bulk} \tag{2}$$

where x_A, x_B are molar fractions of components A and B, ${}^0G_A$, ${}^0G_B$ are the standard Gibbs energies of A and B in a phase [12], R is the gas constant and T is the temperature. $G^{E,Bulk}$ is the excess Gibbs energy of the bulk of phase, expressed usually by Redlich–Kister polynomial

$$G^{E,Bulk} = x_A x_B \sum_n L^n(T)(x_B - x_A)^n \tag{3}$$

where $n = 0, 1, 2, \ldots$ and parameters $L^n(T)$ are temperature dependent:

$$L^n(T) = a_n + b_n T + c_n T \ln(T) \tag{4}$$

The temperature dependent parameters $L^n(T)$ can be extracted from a thermodynamic database [13].

The Gibbs energy of the surface $G^{E,S}$ of phase is expressed for isotropic spherical particles by

$$G^{E,S} = \frac{2C\tau V}{r} \tag{5}$$

where τ is the surface tension, V is the molar volume, r is the radius of the particle and C is the correction factor considering the effects from the shape, the surface strain due to non-uniformity and the uncertainty of the surface tension measurements [4]. The value of C for fcc solid structure and for liquid were estimated to be 1.00 [4].

Surface tension of solid Cu and Ni were calculated by approximation $\tau_i^S = 1.25\tau_i^L$ at melting temperature of pure metals i and $(d\tau_i^S/dT) = (d\tau_i^L/dT)$ [3].

For metallic binary alloys, we can suppose that the molar volume is given by

$$V = x_A V_A + x_B V_B \tag{6}$$

The surface tension of a binary liquid alloy phase can be calculated from the Butler equation [14]

$$\tau = \tau_A + \frac{1}{A_A}(G_A^{E,S} - G_A^{E,Bulk}) + \frac{RT}{A_A}\ln\left(\frac{1-x_B^S}{1-x_B}\right) \tag{7}$$

or

$$\tau = \tau_B + \frac{1}{A_B}(G_B^{E,S} - G_B^{E,Bulk}) + \frac{RT}{A_B}\ln\left(\frac{x_B^S}{x_B}\right) \tag{8}$$

where τ_i is the surface tension of liquid of component i, A_i is the superficial area occupied by the liquid component i, $G_i^{E,Bulk}$ is the partial Gibbs energy of component i in bulk and $G_i^{E,S}$ is the partial Gibbs energy of component i in the surface. For the calculation of surface tension of liquid alloys on this basis, the computer code was written [15].

According to model given in [16], it is assumed that partial surface excess Gibbs energy is related to that of the bulk phase by

$$G_i^{E,S}(T, x_j^S) = \beta^{Mix} G_i^{E,Bulk}(T, x_i^{Bulk}) \tag{9}$$

where β^{Mix} is a parameter corresponding to the ratio of the coordination number in the surface to that in the bulk. Tanaka et al. [17] have shown, that the value of $\beta^{Mix} = \beta^{Pure}$, the same as parameter for pure metals, which can be determined from the relationship

$$\tau_i A_i = (1 - \beta^{Pure})\Delta H_{L-G,i} \tag{10}$$

where A_i is the molar surface area of pure i and $\Delta H_{L-G,i}$ is the heat for liquid–gas transformation of metal i. A similar equation is valid for β^{Pure} for solid, which can be determined from the equation

$$\tau_i A_i = (1 - \beta^{Pure})\Delta H_{S-G,i} \tag{11}$$

with $\Delta H_{S-G,i}$ being the heat for solid–gas transformation of metal i. The values of β^{Pure} in liquid and in solid were estimated to be 0.85 and 0.84, respectively [6]. Therefore, if the differences in shape and surface strain with respect to composition can be ignored, the surface tension of solid alloys can be predicted by the Butler equation [14].

Calculation of a phase diagram continues in two steps. The surface Gibbs energy of nanoalloys consists of two terms: the surface energy of pure components and the surface energy of nanoalloys (see Eqs. (5)–(8)). Both corrections are a function of $(1/r)$, for which we introduce the function "reciprocal radius" (RR).

The temperature dependent surface tension $\tau_i^S(T)$, $\tau_i^L(T)$ and molar volume $V_i^S(T)$, $V_i^L(T)$ are presented in Table 1. Thermodynamic parameters of pure elements and binary parameters for the CALPHAD-type calculation of the phase diagram of Cu–Ni system are listed in the Supplementary file.

The deviation of surface tension of nanoalloys from the linear concentration dependence, assumed in the previous step, are taken into account by calculation of the surface tension of alloys in liquid state and in solid state. These calculations were performed by the Butler Eqs. (7) and (8) [14] implemented in software [15]. Concentration dependence of surface tension for liquid and solid phases at 1400 K is presented in Fig. 1. It is in agreement with [31].

Table 1
Physical properties of Cu and Ni pure elements (L – liquid, S – solid (i.e. fcc) phase).

Surface tension (average values from literature in list: [3,18–25] for Cu, [24,26–31] for Ni):	
$\tau_{Cu}{}^{L}$ (N/m)$=(1.624 \pm 0.481)$–(0.226 ± 0.215) T $\times 10^{-3}$	
$\tau_{Cu}{}^{S}$ (N/m)$=1.9535$–2.26 T $\times 10^{-4}$	
$\tau_{Ni}{}^{L}$ (N/m)$=2.488 \pm 0.389$)–(0.393 ± 0.189) T $\times 10^{-3}$	
$\tau_{Ni}{}^{S}$ (N/m)$=2.940$–3.92 T $\times 10^{-4}$	
Molar:	
$V_{Cu}{}^{L}$ (m^3/mol)$=6.95 \times 10^{-6} + 8.08$ T $\times 10^{-10}$	[26]
$V_{Cu}{}^{S}$ (m^3/mol)$=7.09 \times 10^{-6}$	[1]
$V_{Ni}{}^{L}$ (m^3/mol)$=5.85 \times 10^{-6} + 9.02$ T $\times 10^{-10}$	[32,26]
$V_{Ni}{}^{S}$ (m^3/mol)$=6.60 \times 10^{-6}$	[1]

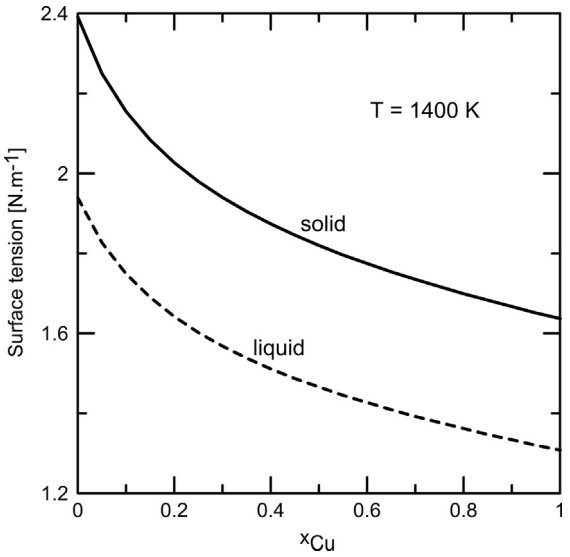

Fig. 1. Concentration dependence of surface tension (surface energy) for liquid and solid phases in the Cu–Ni system at 1400 K calculated by the Butler equation [14] based on average data for pure elements in literature list and thermodynamic data in literature [13].

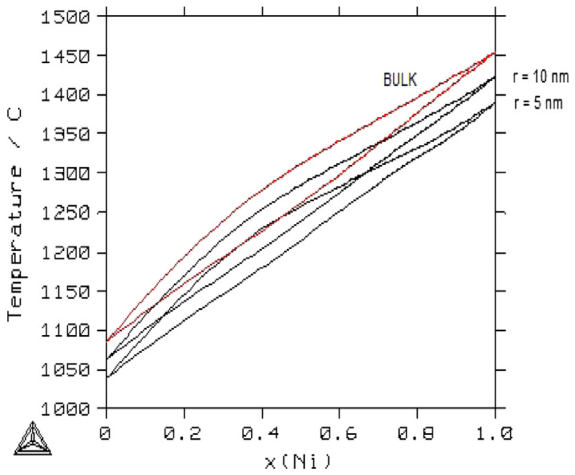

Fig. 2. The phase diagram of the Cu–Ni system for bulk alloys and for nanoalloys of radius $r=5$ nm and $r=10$ nm.

Presented concentration dependence of the surface tension (see Fig. 1) of liquid and solid phase $\tau^L(x_{Cu})$, $\tau^S(x_{Cu})$ multiplied by the (linear) concentration dependence of molar volume $V^L(x_{Cu})$, $V^S(x_{Cu})$ makes it possible to express the concentration dependence of the excess surface Gibbs energy for nanoalloys in both phases (see Eq. (5)) and to approximate it by Redlich–Kister type polynomial, when differences from linear concentration dependence of surface Gibbs energy are taken into account:

$$G^{E,S} = x_A x_B \sum_i L^i(T)(x_B - x_A)^i \quad (i = 0,\ 1,\ 2, \ldots) \tag{12}$$

The result of this procedure is in the supplementary file where it is merged with eqs. in [13]. Phase diagram calculated with the surface energy correction for nanoalloys of radius 10 nm and 5 nm is shown in Fig. 2.

3. Experimental

3.1. Synthesis of Cu–Ni nanoparticles

The Cu–Ni alloy nanoparticles (NPs) of various composition were prepared by solvothermal reaction from nickel acetylacetonate Ni $(acac)_2$ and copper acetylacetonate $Cu(acac)_2$ precursors in a particular stoichiometric ratio under an inert atmosphere of nitrogen [32]. The molecular precursors were dissolved in oleylamine and this solution was injected into a hot solvent composed of 1-octadecen and oleylamine at 230 °C. As a heating bath, Sn–Pb solder was used. In the reaction mixture, the precursor metal cations were reduced by oleylamine at this temperature and formed the Cu–Ni nanoalloy colloid. The product for the DSC, XRD, IR and ICP/OES analysis was separated by precipitation with methanol, centrifugation for 20 min on a Heraeus Labofuge 400 at 3500 rpm and washing with methanol/hexane solution. The powders were washed to remove organic-soluble residues by three cycles of resuspending them in hexane or light petroleum and subsequent centrifugations. Thus the colloidal solution of the Cu–Ni NPs in hexane was prepared. The NPs synthesis was carried out so that the chemical compositions of Cu–Ni samples were outside of the Cu–Ni phase diagram miscibility gap (fcc) [13].

3.2. Nanoparticle characterization

The prepared samples of the Cu–Ni alloy nanoparticles were characterized experimentally by different methods. The corresponding experimental studies performed on the NPs samples presented in this work are given in Table 2.

The size distribution of the Cu–Ni NPs of all samples was measured by the dynamic light scattering (DLS) method immediately after sample synthesis. For this measurement, as well as for TEM analysis, nanoparticles were directly separated from the reaction solution by centrifugation and washed with hexane without the precipitation step with methanol, providing homogeneous colloidal solutions of Cu–Ni nanoparticles in hexane. The hydrodynamic diameter of the Cu–Ni nanoparticles was measured on a Zetasizer Nano ZS ZEN 3500 DLS instrument at the angle of 173° in a hexane solution at 25 °C. The results are based on the intensity of scattered light, the source being He–Ne red laser with a wavelength of 632.8 nm. The measured size distribution maximum of the major peak is in Fig. 3.

The electron microscopy was applied for the size verification of precipitated powders. Transmission electron microscopy (TEM) was carried out on Philips CM12 STEM operated at 120 kV and high resolution transmission electron microscopy (HRTEM) on JEOL JEM3010 microscope operated at 300 kV. Instruments were equipped with a LaB_6 cathode, an EDX (Energy Dispersive X-ray) detector, and characterized by a point-to-point resolution of 1.7 Å. Images were recorded by a CCD camera with resolution of 1024×1024 pixels using the Digital Micrograph software package. Samples were also investigated by TESCAN LYRA 3 XMU FEG/SEM × FIB scanning electron microscope (SEM). Powder samples were dispersed in ethanol and the suspension was treated in ultrasound for 10 min. A drop of very dilute suspension was placed on a carbon-coated grid and allowed to dry by evaporation at ambient temperature. The prepared samples of the Cu–Ni NPs differ in chemical composition

Table 2
The nanoalloys prepared and the corresponding experimental studies performed on them.

Sample	Composition from precursor weights in wt% (alternative methods)	Experimental studies
CuNi12	Cu – 12% Ni (ICP/OES: Cu – 11.1% Ni)	DLS, DSC, TEM, SEM, ICP/OES
CuNi20	Cu – 20% Ni (EDX:Cu – 27%Ni)	DLS, DSC, HRTEM, XRD, EDX
CuNi14	Cu – 14% Ni	DLS, IR
CuNi40	Cu – 40% Ni (EDX: Cu – 43% Ni)	DSC, EDX

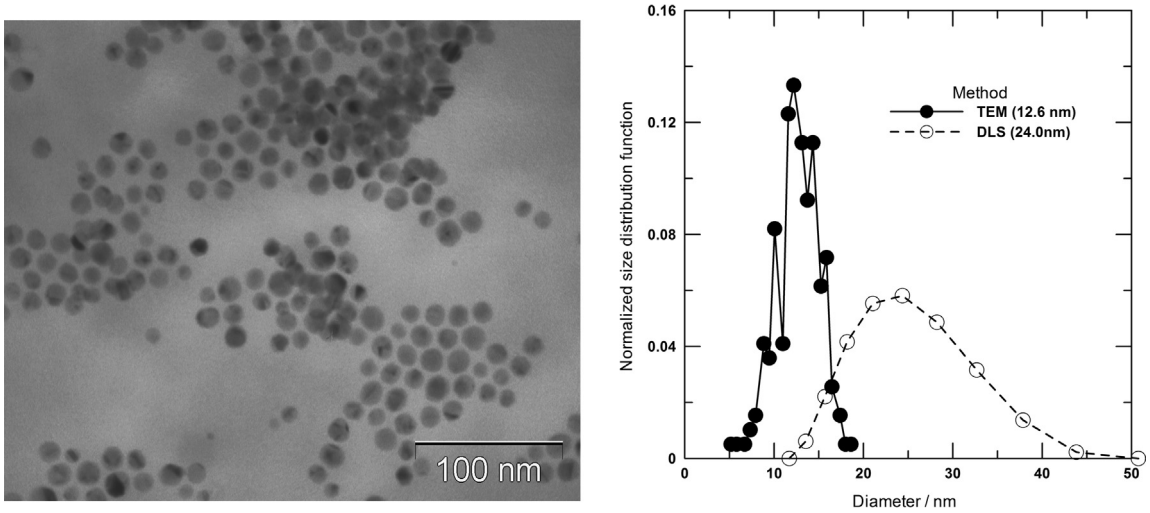

Fig. 3. Particle size distribution of the synthesized CuNi NPs (sample CuNi12, TEM image analysis, DLS).

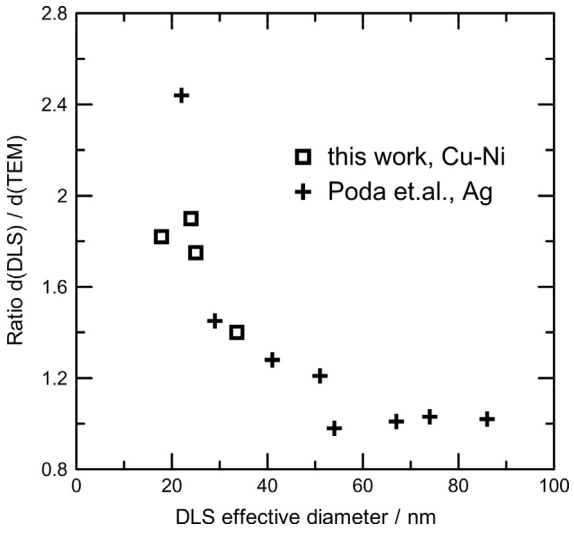

Fig. 4. The dependence of the diameter ratio *d*(*DLS*)/*d*(*TEM*) (i.e. (hydrodynamic diameter *d*(*DLS*) obtained by DLS)/(core size evaluated diameter *d*(*TEM*) from TEM image analysis)) on the DLS effective diameter of Cu–Ni (squares – this work) and Ag (crosses – Poda [33]) nanoparticles determined by DLS.

due to different metallic precursor batches but they have all similar size, shape and morphology. The examples of the TEM pictures are given in Fig. 3 (individual particles) and Fig. 5 (partially aggregated particles). The more detailed view (HRTEM) of the Cu–Ni NPs is in Fig. 6. The transmission electron microscopy TEM/HRTEM analysis revealed the crystalline spherical particles with a relatively narrow size distribution (see Figs. 3 and 5). The difference between nanoparticle hydrodynamic size obtained by DLS and core size revealed by image analysis of the TEM photos is given in Fig. 4. The results will be discussed later in Section 4.

The composition of some synthesized nanoparticle samples after DSC was established by the EDX technique on JEOL 6490 LV instrument equipped with an EDX spectrometer. The accuracy of this technique was not satisfactory but it enabled observation of nanoparticle sensitivity to oxygen. For example CuNi40 sample featured elemental weight concentrations of 3% O, 53% Cu, and 43% Ni before DSC. The oxidation also increased to approx. 5% O (for sample CuNi20 involving 27% Ni, and 68% Cu) after the DSC analysis. These results indicate that Cu–Ni NPs are sensitive to oxygen and the time of manipulation in dry state must be minimized (compare also Fig. 7).

Some of the samples after synthesis of the Cu–Ni NPs were dissolved in nitric acid and analyzed by ICP-OES to evaluate an exact metal content of the Cu–Ni NPs. The accuracy (± 0.02 wt%) of the composition results obtained by ICP/OES is about 10 times better than the accuracy available by EDX microanalysis but more time consuming.

The Cu–Ni NP lattice was investigated by the X-ray diffraction (XRD). A Stoe–Cie transmission diffractometer STADI P operating with a Ge monochromatized Co ($\lambda = 0.1788965$ nm) radiation (40 kV, 30 mA) and equipped with a PSD detector or an X'PertPRO (PANAlytical, b.v. Almelo, The Netherlands) instrument using CoKα radiation (40 kV, 30 mA) and X'Celerator linear PSD detector were used for the XRD data acquisition at room temperature. Powder XRD experiments on the CuNi20 sample revealed broad diffractions (see Fig. 7) corresponding to an fcc structure of Cu (PDF 4-836) [34]. The unit cell refinement provided the lattice constant $a = 0.36058$ nm that falls in the range reported for this composition of Cu–Ni systems [35]. The weak broad diffractions in the range 41–46° 2θ correspond probably to Cu_2O (PDF 5-667) and CuO (PDF 5-661) resulting from a mild surface oxidation [34].

The as-synthesized sample CuNi14 was investigated by infrared spectroscopy. The IR spectra were recorded on a Bruker Tensor T27 FT-IR spectrometer in KBr pellets. The spectrum revealed the presence of organic layer on the surface of nanoparticles (Fig. 8). A broad vibration band at 3423 cm^{-1} corresponds to the NH stretching, bands at 2958, 2923, 2851 cm^{-1} arise from the C–H valence stretching of the aliphatic chains of oleylamine.

3.3. Differential scanning calorimetry (DSC)

Thermal behavior of the Cu–Ni NPs was investigated by the DSC method. The experiments were carried out on a Netzsch DSC STA 409C/QMS instrument under flowing (70 cm^3 min^{-1}) pure (6 N) argon with the heating rate of 10 °C min^{-1} from room temperature to 1250 °C. The samples (approx. 10 mg) were contained in alumina crucibles with a lid. The example of DSC measurement is in Fig. 9.

The thermal effects of the 1st heating cycle and the 3rd heating cycle are in Fig. 9. The heating reveals melting behavior evaluated by standard procedure and exothermal effects. The shift of sample melting to bulk melting point can occur. After DSC analysis, the Cu–Ni micropowder (see Fig. 10) was obtained.

4. Results and discussion

The prepared nanoparticles containing Cu and Ni in different stoichiometric ratios were relatively uniform but their chemical composition was different (see Table 2). The image analysis of the TEM micrographs reveal the core diameter (9–18) nm. The hydrodynamic size of the nanoparticles was up to approx. 20–30 nm (compare Fig. 3). It gives a high thickness of the stabilization layer that surrounds the core (Fig. 4). Interesting agreement exists between size dependent ratio $d(DLS)/d(TEM)$ for our Cu–Ni nanoparticles in hexane and for Ag nanoparticles in aqueous solution according to Poda et al. [33]. Verification of this agreement needs further experimental examination using additional NPs systems.

The effect of absorption of electron beam energy was observed for high accelerating voltage (Fig. 5), which resulted in the formation of larger particles by aggregation. The HRTEM (Fig. 6) shows a uniform lattice of the core. Detected oxygen content in samples was caused by a brief manipulation of samples in air. We believe that there is an oxide layer on the surface but it does not affect the NPs melting.

The lattice constant of nanoparticles of sample CuNi20 ($a=0.36058$ nm) was determined by the XRD measurement (Fig. 7). This experimental lattice constant is within the limit of experimental accuracy in agreement with the value 0.3590 nm calculated using fcc lattice constants (for Cu: 0.36148 nm, Ni: 0.35239 nm) [35] and Vegard's law, which is valid for Cu–Ni bulk alloy [36]. The IR spectrum revealed the presence of organic layer on the surface of nanoparticles (Fig. 8).

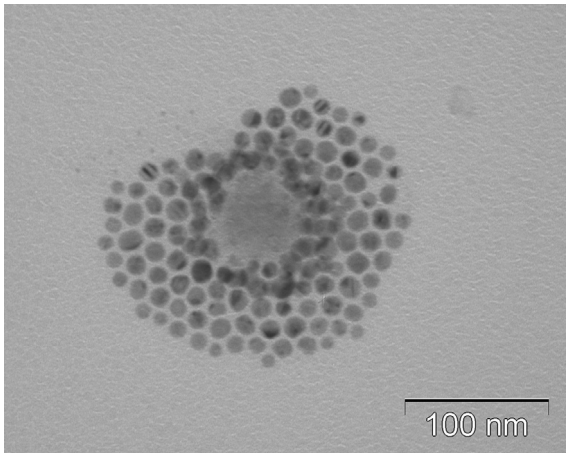

Fig. 5. Micrograph of the synthesized Cu–Ni NPs (sample CuNi12, TEM). The partially aggregated nanoparticles are in the center.

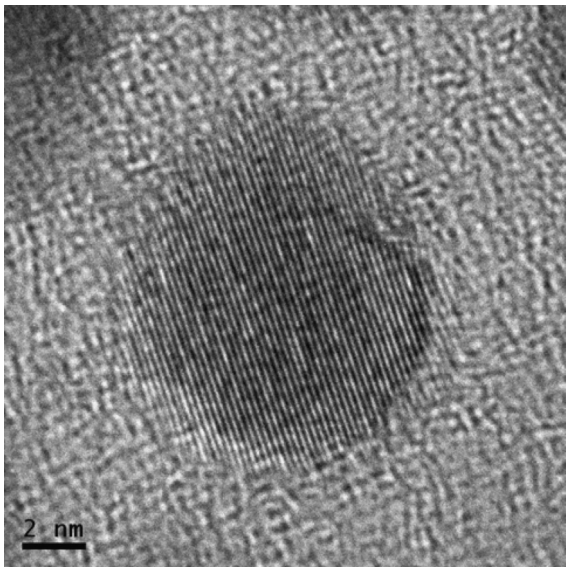

Fig. 6. A single particle of the synthesized CuNi20 nanoalloy (HRTEM, direction [110]).

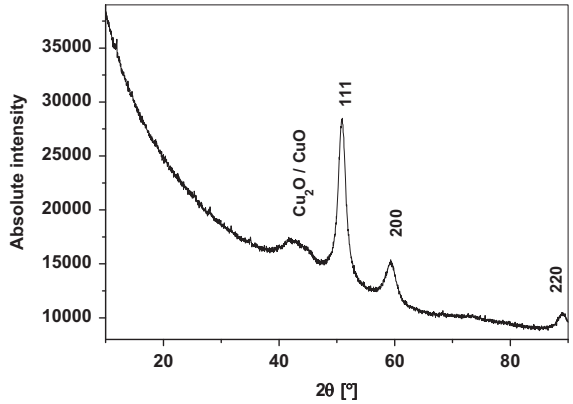

Fig. 7. XRD of the powder CuNi20 nanoalloy (indexes valid for fcc CuNi).

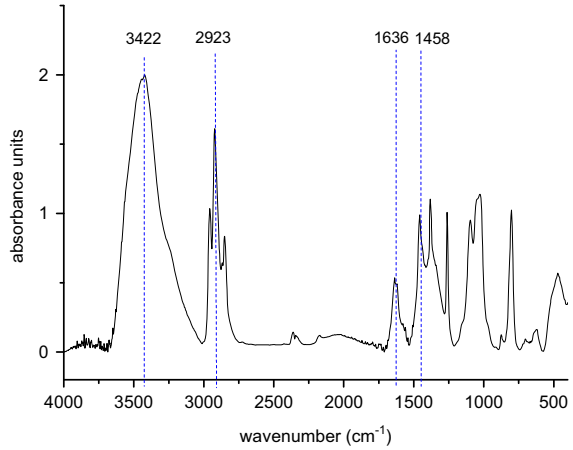

Fig. 8. The IR spectra of the Cu–Ni nanoparticles.

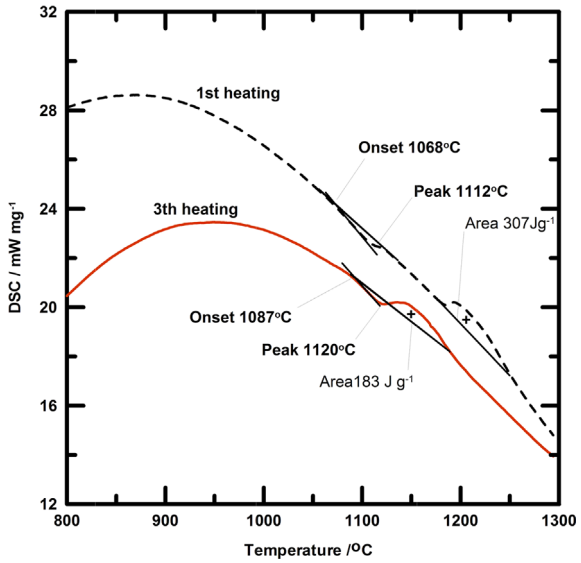

Fig. 9. DSC signal of the CuNi nanopowder (sample CuNi12). 1st heating (dashed line), 3rd heating: (solid line). Symbol "+" mean exothermic effect.

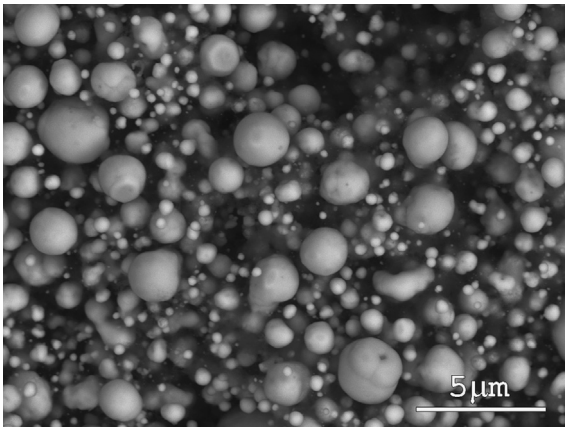

Fig. 10. Micrograph of the CuNi12 sample after DSC analysis (microsized particles, i.e. bulk formed, SEM).

Table 3
Experimental and theoretical (CALPHAD) results on Cu–Ni NPs.

Sample	Ni/(Ni+Cu)	NPs diameter (TEM/DLS) (nm)	Solidus (calculated) (°C)	NPs solidus (DSC onset) (°C)	NPs solidus (calculated) (°C)
CuNi12	11.1 wt% 11.9 at%	12.6/26.0	1130.3	1068	1093

Thermal analysis was used for the determination of changes in the temperature of melting of the Cu–Ni nanoparticles. The Cu–Ni nanoparticles (wet by solvent) were placed in a DSC calorimeter and heated. The DSC signal (Fig. 9) was measured. Above the melting temperature, further effects were observed. These effects can be explained as coagulation of Cu–Ni nanodroplets to microdroplets (Fig. 10). A comparison of the experimental results with prediction (Fig. 2) is presented in Table 3. An agreement of the CALPHAD type prediction of phase diagram of Cu–Ni NPs with the experimental data is satisfactory if we consider all approximations and that the nucleation process is not involved.

5. Conclusions

Stabilized Cu–Ni nanoparticles were prepared by wet synthesis from metal precursors. The nanoparticles formed from an uniform metal core and stabilizing organic shell were prepared. The particles were characterized by different physical methods. The experimental results on the Cu–Ni nanoparticles show reasonable consistency. The size dependent predicted phase diagram of Cu–Ni system was calculated by the CALPHAD method with considering surface energies of the nanoparticles. The CALPHAD method can be recommended for planning experiments connected with applications of nanoparticles.

Acknowledgments

Financial support of the Ministry of Education of the Czech Republic under the project LD 11046 (within COST MP0903 Action), RVO: 68081723, and CEITEC-MU CZ.1.05/1.1.00/02.0068 are gratefully acknowledged.

Appendix A. Supplementary materials

Supplementary data associated with this article can be found in the online version at http://dx.doi.org/10.1016/j.calphad.2013.11.004.

References

[1] A. Shirinyan, M. Wautelet, Y. Belogorodsky, Solubility diagram of the Cu–Ni nanosystem, J. Phys. Condens. Mater. 18 (2006) 2537–2551.
[2] S.P. Huang, P.B. Balbuena, Melting of bimetallic Cu–Ni nanoclusters, J. Phys. Chem. B. 106 (2002) 7225–7236.
[3] T. Tanaka, S. Hara, Thermodynamic evaluation of binary phase diagrams of small particles systems, Z. Metallkd. 92 (2001) 467–472.
[4] J. Lee, T. Tanaka, J.G. Lee, H. Mori, Effect of substrates on the melting temperature of gold nanoparticles, CALPHAD 31 (2007) 105–111.
[5] W.A. Jesser, R.Z. Schneck, W.W. Gile, Solid-liquid equilibria in nanoparticles of Pb–Bi alloys, Phys. Rev. B 69 (144121-) (2004) 1–13.
[6] J. Park, J. Lee, Phase diagram reassessment of Ag–Au system including size effect, CALPHAD 32 (2008) 135–141.
[7] S.L. Chen, S. Daniel, F. Zhang, Y.A. Cang, X.-Y. Yan, F.-Y. Xie, R. Schmid-Fetzer, W.A. Oates, The PANDAT software package and its applications, CALPHAD 26 (2002) 175.
[8] C.W. Bale, P. Chartrand, S.A. Degterov, G. Erikson, K. Hack, R. Ben, J. Melancon, A.D. Pelton, S. Petersen, FactSage thermochemical software and databases, CALPHAD 26 (2002) 189–228.
[9] R.H. Davies, A.T. Dinsdale, J.A. Gisby, J.A.J. Robinson, S.M. Martin, MTDATA – thermodynamic and phase equilibrium software from the national physical laboratory, CALPHAD 26 (2002) 229–271.
[10] J.O. Anderson, T. Helander, L. Hoglund, P. Shi, B. Sundman, Thermo-Calc & DICTRA, computational tools for materials science, CALPHAD 26 (2002) 273–312.
[11] J. Feng, C.P. Zhang, Preparation of Cu–Ni alloy nanocrystallites in water-in-oil microemulsions, J. Colloid Interface Sci. 293 (2006) 414–420.
[12] A.T. Dinsdale, SGTE data for pure elements, CALPHAD 15 (1991) 317–425.
[13] S.A. Mey, Thermodynamic re-evaluation of the Cu–Ni system, CALPHAD 16 (1992) 255–260.
[14] J.A.V. Butler, The thermodynamics of the surfaces of solutions, Proc. R. Soc. A 135 (1932) 348–375.
[15] R. Picha, J. Vrestal, A. Kroupa, Prediction of alloy surface tension using a thermodynamic database, CALPHAD 28 (2004) 141–146.
[16] I. Egry, E. Ricci, R. Novakovic, S. Ozawa, Surface tension of liquid metals and alloys – recent developments, Adv. Coloid Interface Sci. 159 (2010) 198–212.
[17] T. Tanaka, K. Hack, T. Iida, S. Hara, Application of thermodynamic databases to the evaluation of surface tensions of molten alloys, salt mixtures and oxide mixtures, Z. Metallkd. 87 (1996) 380–389.
[18] G. Lang, P. Laty, J.C. Joud, P. Desre, Measurement of the surface tension of some fluid metals by different methods, Z. Metallkd. 68 (1977) 113–116.
[19] B.M. Lepinskikh, Doc. VINITI, USSR 4/5 (1979) 1918–1979.
[20] P. Darrell-Ownby, J. Lui, Surface energy of liquid copper and single-crystal sapphire and the wetting behavior of copper on sapphire, J. Adhes. Sci. Technol. 2 (1988) 255–269.
[21] K. Nogi, K. Oishi, K. Ogino, Wettability of solid oxides by liquid pure metals, Mater. Trans. JIM 30 (1989) 137–145.
[22] J. Lee, W. Shimoda, T. Tanaka, Surface tension and its temperature coefficient of liquid Sn–X (X=Ag, Cu) alloys, Mater. Trans. 45 (2004) 2864–2870.
[23] Z. Moser, W. Gasior, J. Pstrus, Influence of Sb additions on surface tension and density of Sn–Sb, Sn–Ag–Sb and Sn–Ag–Cu–Sb alloys. Experiment vs. modeling, Int. J. Mater. Res. 97 (2006) 365–370.
[24] R. Brooks, I. Egry, S. Seetharaman, Reliable data for high-temperature viscosity and surface tension: results from European project, High Temp.–High Press 33 (2001) 631–637.
[25] I. Egry, J. Brillo, Surface tension and density of liquid metallic alloys measured by electromagnetic levitation, J. Chem. Eng. Data 54 (2009) 2347–2352.
[26] G. Lohöfer, J. Brillo, I. Egry, Thermophysical properties of undercooled liquid Cu–Ni alloys, Int. J. Thermophys. 25 (2004) 1535–1550.
[27] F. Xiao, R. Yang, Ch. Zhang, Surface tension of molten Ni–W and Ni–Cr alloys, Mater. Sci. Eng. B 132 (2006) 183–186.
[28] F. Xiao, L.-X. Liu, R.-H. Yang, H.-K. Zhao, L. Fang, Ch. Zhang, Surface tension of molten Ni–(Cr,Co,W) alloys and segregation of elements, Trans. Nonferrous Met. Soc. China 18 (2008) 1184–1188.
[29] H.Y. Hou, G.L. Chen, G. Chen, Y.L. Shao, A molecular dynamic simulation on surface tension of liquid Ni and Cu, Comput. Mater. Sci. 46 (2009) 516–519.
[30] S.D. Korkmaz, S. Korkmaz, Investigation of surface properties of liquid transition metals: surface tension and surface entropy, Appl. Surf. Sci. 257 (2010) 261–265.
[31] J. Brillo, I. Egry, Surface tension of nickel, copper, iron and their binary alloys, J. Mater. Sci. 40 (2005) 2213–2216.
[32] Y. Zhang, W. Huang, S.E. Habas, J.N. Kuhn, M.E. Grass, Y. Yamada, P. Yang, G.A. Somorjai, Near-monodisperse Ni–Cu bimetallic nanocrystals of variable composition: controlled synthesis and catalytic activity for H_2 generation, J. Phys. Chem. C 112 (2008) 12092–12095.
[33] A.R. Poda, A.J. Bednar, A.J. Kennedy, A. Harmon, M. Hull, D.M. Mitrano, J.F. Ranville, J. Steevens, Characterization of silver nanoparticles using flow-

field flow fractionation interfaced to inductively coupled plasma mass spectrometry, J. Chromatogr. A 1218 (2011) 4219–4225.
[34] JCPDS PDF-2 database, International Centre for Diffraction Data, Newtown Square, PA, USA, 1996.
[35] ICSD database FIZ Karlsruhe, Germany, release 2012/1, 2012.
[36] L.E. Cratty, W.W. Russell, Nickel, copper and some of their alloys as catalysts for the hydrogenation of carbon dioxide, J. Am. Chem. Soc. 80 (1957) 767–773.